Grain boundary energy effect on grain boundary segregation in an equiatomic high-entropy alloy

Linlin Li,[1,2,*,†] Reza Darvishi Kamachali,[1,3,*] Zhiming Li,[1,4,‡] and Zhefeng Zhang[2]
[1]*Max-Planck-Institut für Eisenforschung, Max-Planck-Straβe 1, 40237 Düsseldorf, Germany*
[2]*Institute of Metal Research, Chinese Academy of Science, Wenhua Road 72, Shenyang 110016, People's Republic of China*
[3]*Federal Institute for Materials Research and Testing (BAM), Unter den Eichen 87, 12205 Berlin, Germany*
[4]*School of Materials Science and Engineering, Central South University, Changsha 410083, China*

(Received 17 January 2020; accepted 21 April 2020; published 29 May 2020)

Grain boundary (GB) segregation has a substantial effect on the microstructure evolution and properties of polycrystalline alloys. The mechanism of nanoscale segregation at the various GBs in multicomponent alloys is of great challenge to reveal and remains elusive so far. To address this issue, we studied the GB segregation in a representative equiatomic FeMnNiCoCr high-entropy alloy (HEA) aged at 450 °C. By combining transmission Kikuchi diffraction, atom probe tomography analysis and a density-based thermodynamics modeling, we uncover the nanoscale segregation behavior at a series of well-characterized GBs of different characters. No segregation occurs at coherent twin boundaries; only slight nanoscale segregation of Ni takes place at the low-angle GBs and vicinal Σ29*b* coincidence site lattice GBs. Ni and Mn show cosegregation of high levels at the general high-angle GBs with a strong depletion in Fe, Cr, and Co. Our density-based thermodynamic model reveals that the highly negative energy of mixing Ni and Mn is the main driving force for nanoscale cosegregation to the GBs. This is further assisted by the opposite segregation of Ni and Cr atoms with a positive enthalpy of mixing. It is also found that GBs of higher interfacial energy, possessing lower atomic densities (higher disorder and free volume), show higher segregation levels. By clarifying the origins of GB segregations in the FeMnNiCoCr HEA, the current work provides fundamental ideas on nanoscale segregation at crystal defects in multicomponent alloys.

DOI: 10.1103/PhysRevMaterials.4.053603

I. INTRODUCTION

Polycrystalline materials generally consist of a large number of grain boundaries (GBs) with various characters. In the GB region, atoms are shifted from their regular lattice sites to accommodate the mismatch between the adjacent grains [1]. Hence, GBs are of higher-energy state compared to the grain interior. To minimize their energy, GBs interact with solute or impurity atoms, resulting in segregation of those atoms to the GB region [2]. Such GB segregation is of particular concern because it largely affects many properties of the polycrystalline materials [3–12]. Segregation of some deleterious elements such as S and Bi to GBs in Ni, for instance, could alter the atomic bonds in the GB region, decrease the atomic cohesion, and promote intergranular fracture [4,5]. On the contrary, segregation of a proper degree of B to GBs can increase the strength and ductility of alloys by enhancing the GB cohesion [6–8]. Also, segregation of Ti to W GBs [9] and segregation of Mo to Ni GBs [10] significantly increase the hardness of the nanostructure by stabilizing the GBs and restraining the GB-mediated softening process.

GB precipitation is another example where the segregation is believed to play a critical role [13,14]. In classical nucleation theory, GBs are more favored nucleation sites than the grain interior as their interfacial energy provides an extra driving force [15]. In Fe-Mn steels, soft austenite layers form among the hard martensite crystals due to Mn segregation to the GBs [16,17] and can serve as mechanical buffer zones to cracking to improve material ductility [18]. Recent atom probe tomography (APT) studies suggest that the phase transformation along the GBs can also occur in a way of spinodal decomposition with the aid of solute segregation [17,19,20]. All the above facts point to a chemical platform for engineering GBs through the solute segregation. Hence, it is crucial to obtain a clear understanding on the mechanisms of the segregation and possible phase separation and transition at GBs.

Based on the Gibbs adsorption isotherm, GB segregation can relate with different thermodynamic and structural variables of the system [21–24]. For instance, the positive mixing enthalpy between solute and solvent atoms [3,23], which is closely related to the bulk solubility [25], increases the segregation tendency of the solute element [26]. Besides the nature of solute and solvent atoms, the structures of GBs, including the index of the GB plane and the misorientation angle, can influence GB segregation [21,22,27–31]. In an Fe-P alloy, the enrichment of P was found to be more significant

*These authors contributed equally to this work.
†l.li@mpie.de
‡zhiming.li@mpie.de

Published by the American Physical Society under the terms of the Creative Commons Attribution 4.0 International license. Further distribution of this work must maintain attribution to the author(s) and the published article's title, journal citation, and DOI. Open access publication funded by the Max Planck Society.

at the GB planes with high indices compared to that at GB planes with lower indices (e.g., {001}, {011} and {112}) [28]. Very low or even no segregation has been observed at coherent twin boundaries (TBs) in the cases of Cu in Pb [29] and Bi in Cu [30]. In fact, GB energy is also closely related to the various GB structures [1,32] and influences the thermodynamic driving force for GB segregation [21,33,34]. Yet, the connection between GB energy and the chemical composition of individual GBs has not been straightforwardly established.

In practice, most engineering materials contain more than one alloying element of high concentrations. In the past decades, high-entropy alloys (HEAs), with multiple elements of similar fractions [35,36], have been introduced showing excellent mechanical properties including high strength and good ductility [37,38]. Elemental partitioning or phase separations can occur in HEA systems [36,39], even in the equiatomic FeMnNiCoCr alloy, a representative single-phase HEA of face-centered-cubic lattice structure [40,41]. After very long annealing of 500 d at medium temperatures (e.g., 500 and 700 °C), second-phase precipitates including NiMn, FeCo, and Cr-rich phases form at GBs in the coarse-grained FeMnNiCoCr alloy [40]. GB segregation also occurs in such multicomponent alloy systems to alter the GB properties and structure significantly [42–44]. The interactions among multiple principal elements and GBs of different characters endow the elemental segregation to GBs with a far more complex route [23,45,46]. Little or no knowledge about GB segregation, especially for substitutional elements to segregate at the various GBs in HEAs, is available. Therefore, to investigate the chemical compositions of individual GBs in HEAs is both scientifically interesting and technically important.

In the present work, we systematically studied the nanoscale segregation at GBs of several typical characters (i.e., low-angle GBs, high-angle GBs, and coincidence site lattice (CSL) GBs] in the equiatomic FeMnNiCoCr HEA by combining transmission Kikuchi diffraction (TKD), APT analysis, and thermodynamics modeling. We employed APT technique to systematically investigate the chemistry (segregation elements, level, and the in-plane segregation patterns) of different types of GBs, including low-angle GB, coherent TB, and general high-angle GBs. All GBs were well characterized by TKD technique. In order to understand the origin of the differences in nanoscale segregation at GBs of different types, we applied a thermodynamic model using a relative atomic density parameter and its spatial gradients to describe GBs with respect to the corresponding bulk. Based on this model, a relationship was established between the segregation level and the initial GB energy that closely depends on the GB misorientation. We discussed the role of ideal segregation energy and mixing enthalpy of different solute atoms for the elemental segregation to GBs of different characters. The present work expands the knowledge on GB segregation in multicomponent alloy systems and provides insights for engineering GBs to optimize material microstructure and properties.

II. METHODOLOGY

A. Sample preparation

The equiatomic FeMnNiCoCr alloy was cast in a vacuum induction furnace with high-purity metals. The exact chemical composition of this alloy is Fe-18.9-Mn-19.9Ni-20.6Co-20.1Cr-20.5 in atomic ratio based on wet-chemical analysis. Hot rolling at 900 °C and heat treatment at 1200 °C in Ar atmosphere for 2 h were employed to homogenize the alloy plate. The homogenized material was cold rolled with a thickness reduction of 60% and then annealed at 900 °C for 10 min in Ar atmosphere. To induce GB segregations, the annealed alloy was aging heat treated at 450 °C for 18 h. All heat treatments were followed by water quenching.

B. Microstructural characterization

The microstructure of bulk sample was detected by electron backscattered diffraction (EBSD) method in a Zeiss 1540 XB scanning electron microscope. The EBSD measurements were performed with the acceleration voltage of 15 kV, aperture size of 120 μm, working distance of 13 mm, and step size of 0.8 μm. Needle-shaped APT tips were fabricated using a dual-beam focused-ion-beam (FIB) instrument (FEI Helios Nanolab600i) by an *in situ* lift-out method [47]. The APT tips were prepared from positions with specific GBs according to prior EBSD characterization. During sharpening of the APT tips, the TKD technique embedded in the FIB system was employed to trace the GB position as well as further confirm the GB characters. The TKD tests were performed with the accelerate voltage of 20 KV, beam current of 1.4 nA, working distance of 4 mm, and step size of 10–20 nm. APT Instrument of LEAPTM 3000X HR by Cameca was employed to investigate the chemical composition for all samples at the atomic scale. About 3 APT samples were prepared and tested for each GB. The measurements were performed in voltage mode at 70 K, with a pulse fraction of 15%, a pulse rate of 200 kHz, and a target detection rate of 0.4% (4 detection events per 1000 pulses in average). IVAS® 3.8.2 software was employed for all the reconstruction of three-dimensional atom maps, visualization, and all data analysis.

C. Density-based thermodynamic model for GB segregation

To understand the dependency of segregation on GB nature, we employ a density-based thermodynamic model to describe GBs. This model has been recently introduced [48] and successfully applied in studying GB segregation and interfacial spinodal in FeMn alloys [49]. Because of their defected structures, GBs possess excess free volumes and thus lower average densities with respect to their corresponding bulk material. The key parameter of the current model is a relative atomic density field ρ which varies as $\rho^{GB} \leqslant \rho < \rho^{B} = 1$ across the GB region. For a flat GB centered at position $x = x_0$, $\rho(x \geqslant \pm\eta) = 1$ is the relative bulk density and $\rho(x = x_0) = \rho^{GB} < 1$ is the relative GB density value corresponding to the GB plane. Here η is the GB half-width. There can be, therefore, a relationship established between the GB and bulk properties when described as a function of this relative atomic density profile.

Using the density-based free-energy formulation [48], the Gibbs free energy of the GB can be approximated based on the available thermodynamic data for its corresponding bulk phase. For a binary regular solution made of solvent A and

solute B atoms, the Gibbs energy reads

$$G(X_B,\rho) = X_A\left(E_A^B\rho^2 + \left(K_A^B + pV_A^B - TS_A^B\right)\rho\right) + X_B\left(E_B^B\rho^2 + \left(K_B^B + pV_B^B - TS_B^B\right)\rho\right) + \rho^2\Omega\, X_AX_B + RT[X_A\ln X_A + X_B\ln X_B], \quad (1)$$

where the superscript B represents the bulk properties and the subscripts A and B represent the solvent and solute atoms, respectively. Here, Ω is the mixing enthalpy coefficient, T is temperature, X_i is the molar fraction, E_i^B is the potential energy, K_i^B is the kinetic energy, pV_i^B is the mechanical energy, $H_i^B = E_i^B + K_i^B + pV_i^B$ is the enthalpy, and S_i^B is the entropy of the pure system made of i atoms. In this study, we are interested in a material point within the GB plane where $\rho(x = x_0) = \rho^{GB}$. For this point, the gradient energy terms discussed by van der Waals [50] and Cahn and Hilliard [51] can be neglected for simplicity [48]. The bulk and GB Gibbs free energy will be $G^B = G(X_B^B, 1)$ and $G^{GB} = G(X_B^{GB}, \rho^{GB})$, respectively. For the mixing enthalpy coefficient, we make use of the first-neighbor approximation [52]:

$$\Omega = N_aZ\left(\epsilon_{AB} - \frac{\epsilon_{AA} + \epsilon_{BB}}{2}\right), \quad (2)$$

where N_a is Avogadro number, Z is the coordination number, ϵ_{ij} is the bonding energy between atoms i and j, and $X_A(X_B)$ is the mole fraction of atoms A (B) with $X_A + X_B = 1$.

For a flat GB in a pure substance made of atoms A, the GB energy can be derived using the density-based model as [48]

$$\gamma = \alpha_0(1 - \rho^{GB})^2. \quad (3)$$

Here α_0 is a material constant and ρ^{GB} is the GB density. For any given GB, ρ^{GB} is a characteristic property of the GB, related to its excess free volume, which can be measured either theoretically or experimentally. The relationships between GB excess free volume, energy, and misorientation angle are extensively discussed in the literature. Aaron and Bolling [53] have shown that generally the GB excess free volume, ΔV increases with the misorientation angle that also results in a higher GB energy. This picture is consistent with Eq. (3) where a lower GB density results in a higher GB energy. In fact, it has been shown that [48]

$$\Delta V \propto (1 - \rho^{GB}), \quad (4)$$

which allows one to establish the connection between the density-based model and previous studies on the GB excess volumes (see Ref. [48] for more details). Through this connection we can investigate the relationship between the GB density ρ^{GB} and the misorientation angle of the GBs (with the exception of special GBs) as discussed in Sec. V.

The thermodynamic equilibrium requires equality of the relative chemical potentials $\mu_B^B - \mu_A^B = \mu_B^{GB} - \mu_A^{GB}$ across the system. This requirement was first discussed by Langmuir-McLean [54] and Fowler-Guggenheim [55], also known as the parallel tangent construction, and later used for studying GB segregation in different materials. Using these conditions applied to Eq. (1) and assuming that the GB density does not change during segregation we find the segregation isotherm

$$\frac{X_B^{GB}}{1 - X_B^{GB}} = \frac{X_B^B}{1 - X_B^B}\cdot\exp\left(-\frac{[\Delta E^B + \Omega]\left(\rho^{GB^2} - 1\right) + (\Delta K^B + p\Delta V^B - T\Delta S^B)(\rho^{GB} - 1) + 2\Omega\left[X_B^B - \rho^{GB^2}X_B^{GB}\right]}{RT}\right), \quad (5)$$

where X_B^{GB} is the composition of the GB at its center ($\rho = \rho^{GB}$), $\Delta E^B = E_B^B - E_A^B$, $\Delta K^B = K_B^B - K_A^B$, $\Delta V^B = V_B^B - V_A^B$, and $\Delta S^B = S_B^B - S_A^B$. For $\Omega = 0$, Eq. (5) reduces to the Langmuir-McLean isotherm [54]:

$$\frac{X_B^{GB}}{1 - X_B^{GB}} = \frac{X_B^B}{1 - X_B^B}\cdot\exp\left(-\frac{\Delta E^B\left(\rho^{GB^2} - 1\right) + (\Delta K^B + p\Delta V^B - T\Delta S^B)(\rho^{GB} - 1)}{RT}\right). \quad (6)$$

Combining Eqs. (3) and (5) then

$$\frac{X_B^{GB}}{1 - X_B^{GB}} = \frac{X_B^B}{1 - X_B^B} \times \exp\left(-\frac{[\Delta E^B + \Omega]\left(\left[1 - \sqrt{\frac{\gamma}{\alpha_0}}\right]^2 - 1\right) + (\Delta K^B + p\Delta V^B - T\Delta S^B)\left(\left[1 - \sqrt{\frac{\gamma}{\alpha_0}}\right] - 1\right) + 2\Omega\left[X_B^B - \left[1 - \sqrt{\frac{\gamma}{\alpha_0}}\right]^2 X_B^{GB}\right]}{RT}\right), \quad (7)$$

which gives the GB segregation X_B^{GB} as a function of bulk composition X_B^B as well as initial GB energy γ. Equations (5) and (7) resemble the well-known Fowler-Guggenheim isotherm [55] but also take the effect of initial GB energy on the segregation into account. The current-density based model for GBs allows a quantitative approximation of GB properties based on the available bulk thermodynamic data. For further information see Refs. [48,49]. Here we make use of this model in studying the dependence of GB segregation on the GB energy.

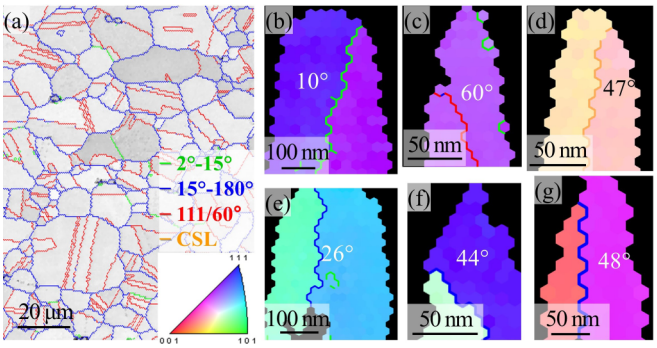

FIG. 1. (a) The image quality (IQ) and grain boundary (GB) map of the HEA aged at 450 °C for 18 h; the inverse pole figure (IPF) along the sample axis and GB maps of the APT sample with (b) a low-angle GB of 10°, (c) a TB of 60°, (d) a vicinal Σ29*b* GB of 47°, (e) a high-angle GB of 26°, (f) a high-angle GB of 44°, and (g) a high-angle GB of 48°.

III. RESULTS

A. Characters of GBs in the annealed plus aged alloy

After aging for 18 h at 450 °C, no new phase is detected and the alloy remains single phase with an average grain size of ∼9 μm according to EBSD analysis. Figure 1(a) shows the image quality (IQ) and GB character map of the aged bulk sample. Since the sample has been fully recrystallized, there are only very few low-angle GBs (<15°) with a fraction as low as ∼3%. The rest of the GBs with higher misorientation angles (>15°) are mainly composed of general high-angle GBs (∼42%) and special (i.e., CSL) GBs (∼54%). The majority of the CSL GBs are Σ3 TBs that occupy ∼50% and the other CSL GBs of higher Σ values only occupy 4%. APT samples containing low-angle GBs, CSL GBs, and general high-angle GBs with different misorientation angles were prepared. Figures 1(b)–1(f) show the inverse pole figure (IPF) and GB character maps of the APT samples detected during the preparation process through TKD. There are a low-angle GB with the misorientation angle of 10° [Fig. 1(b)], a coherent TB [Fig. 1(b)], and a vicinal Σ29*b* GB with the misorientation angle of about 47° [Fig. 1(d)]. Several general high-angle GBs were probed and three of them are displayed representatively here. Their misorientation angles are about 26° [Fig. 1(e)], 44° [Fig. 1(f)], and 48° [Fig. 1(g)], respectively.

B. Segregations to low-angle GB and special high-angle GBs

Figure 2 displays the APT reconstruction from a low-angle GB. Based on the orientations of the two grains on both sides of the GB, the present low-angle GB is not just tilt or twist, but a mixed GB. Figure 2(a) shows the atomic map of interstitial impurities C (∼0.04 at. %) and B (∼0.002 at. %) enriched at the GB, which is consistent with the previous studies that impurity C and B atoms easily segregate to the GBs [7,56]. Isocomposition analysis was also applied to the APT datasets as it can isolate blocks within a specific range of compositions [57]. The typical Ni 25 at. % isocomposition surfaces viewed with the GB edge on in Fig. 2(b) and from the GB plane normal in Fig. 2(c) indicate that the principal element, Ni, can also segregate to the GB. The very few Ni segregations

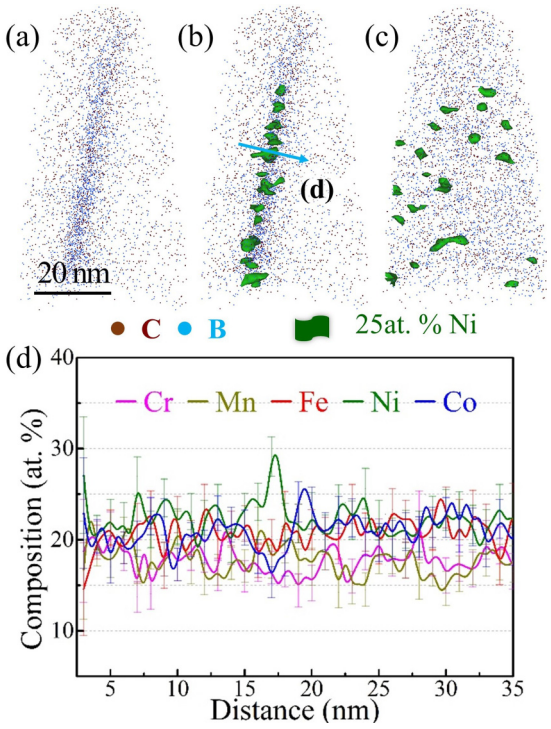

FIG. 2. (a) The atom map of the tip containing a low-angle GB with C and B atoms, Ni 25 at. % isocomposition surfaces (b) viewed with the low-angle GB edge on and (c) viewed along the normal of the GB plane, and (d) the *z* composition along the direction in (b).

assume the form of isolated small regions distributed sparsely and randomly within the GB plane [Fig. 2(c)]. Ni segregation to the low-angle GB with a little increase in its GB concentration (the peak value is ∼28 at. %) is indicated by the one-dimensional (1D) composition profile along the cyan arrow across the GB in Fig. 2(d).

Figure 3 shows the APT analysis results for a coherent TB. The TBs have usually been found to be low or free of segregations due to their perfect interface structure and low energy [58–60]. Indeed, we did not observe any segregation at the TBs in the present alloy either. The homogeneous atom map in Fig. 3(a) reveals that the impurity C or B does not segregate to the TB. With the help of volume render map of Ni [Fig. 3(b)], the position of the TB can be identified in accordance with the TKD observation in Fig. 1(d). The Ni 25 at. % isocomposition surfaces viewed with the TB edge on in Fig. 3(c) and along the normal of the TB plane in Fig. 3(d) show that tiny Ni segregation regions of few nanometers in size appeared at only a part of the TB plane. The 1D composition profile across the TB in Fig. 3(e) also evidences the extremely low segregation of Ni (the maximum GB concentration is ∼26.5 at. %).

Figure 4 reveals the distributions of principal elements near a special CSL GB. The GB has some deviations of about 1–4° from the Σ29*b* GB based on the TKD detection. C and B segregations to the GB mark the GB position clearly in Fig. 4(a). When viewed with the GB edge on, the Ni 25 at. % isocomposition surface in Fig. 4(b) evidences that there is also Ni segregation at the Σ29*b* GB. The 1D composition profile in Fig. 4(c) across the GB indicates that Ni enriches to a

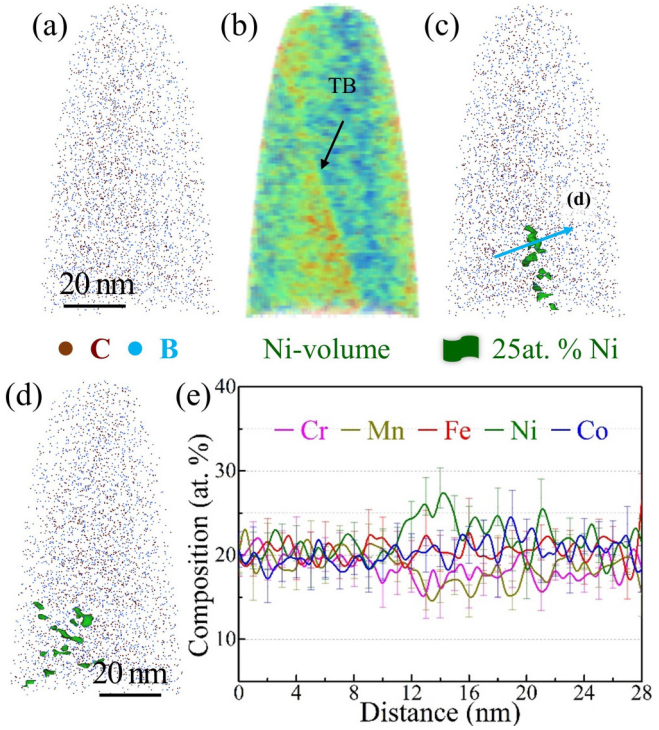

FIG. 3. (a) The atom map of the tip containing a TB with C and B atoms, (b) volume render map of Ni isosurface, Ni 25 at. % isocomposition surfaces (c) viewed with the TB edge on, and (d) viewed from the normal of the TB, and (e) the z composition along the direction in (c).

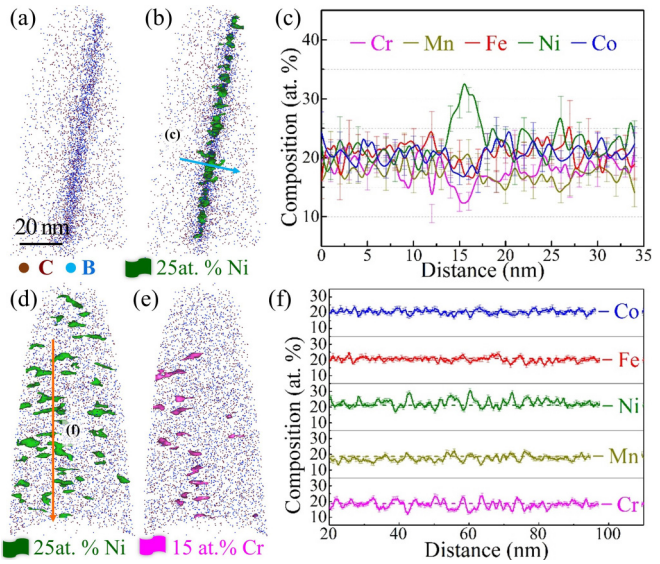

FIG. 4. (a) The atom map of the tip containing a vicinal Σ29b GB with C and B atoms, (b) the Ni 25 at. % isocomposition surfaces, (c) the 1D composition profile along the direction in (b); (d) the Ni 25 at. % isocomposition surfaces, and (e) Cr 15 at. % isocomposition surfaces in the GB plane and (f) the 1D composition profile along the direction indicated in (d); the dashed lines indicate the corresponding bulk compositions. (a), (b) is viewed with the GB edge on and (d), (e) is viewed along the normal of the GB plane.

peak concentration of ∼31 at. % with a little Cr depletion at the Σ29b GB. It is evident that the Σ29b GB [(Fig. 4(c)] has much higher Ni segregation than the Σ3 TB [Fig. 3(e)] consistent with former results that the GBs of higher Σ values usually possess higher segregations [61]. The Ni segregation and Cr depletion along the Σ29b GB plane are clearer when viewed from the normal of the GB plane by the Ni 25 at. % [Fig. 4(d)] and Cr 15 at. % [Fig. 4(e)] isocomposition surfaces. The regions of Ni segregation and Cr depletion are distributed sparsely and homogeneously along the GB plane. Figure 4(f) shows the 1D composition profile of all elements along the orange arrow in Fig. 4(d) within the Σ29b GB plane. Each dashed line in Fig. 4(f) represents the corresponding bulk composition of the element. Fe, Co, and Mn possess relatively stable GB compositions with tiny fluctuations around their bulk compositions. Ni shows segregation while Cr shows depletion both of low levels. Ni and Cr usually repel each other at the GB as at regions where Ni segregates, Cr shows some depletion.

C. Segregations to general high-angle GBs

Figure 5(a) shows the segregation of impurity C and B at the general high-angle GB of 26° as detected before [20]. There is also Ni enrichment at the GB as shown by the Ni 25 at. % isocomposition surface in Fig. 5(b). Figure 5(c) shows the 1D composition profile across this general high-angle GB. Ni enriches obviously (the peak GB concentration is ∼35.7 at. %) together with the depletion of Cr. These phenomena are also accompanied by slight Mn segregation [the local peak GB concentration can reach ∼24.1 at. % as shown in Fig. 5(c)] and Fe, Co depletion. The in-plane views of the respective Ni 25 at. % [Fig. 5(d)] and Cr 15 at. % isocomposition surfaces [Fig. 5(e)] at the GB indicate that Ni segregation or Cr depletion does not occur along the entire but just some separated regions of the GB. More importantly, Ni segregation and Cr depletion form at the same region of the GB as shown vividly by Figs. 5(d) and 5(e) as well as further quantitatively proved by the 1D composition profile within the GB plane in Fig. 5(f).

C and B also segregate to the general high-angle GB of 44° in Fig. 6(a). The edge-on view of the GB with Ni 25 at. % isocomposition surface in Fig. 6(b) indicates that Ni also accumulates at the GB. The 1D composition profile across the GB in Fig. 6(c) shows that there is a large increase of Ni concentration (the peak GB concentration is ∼43.3 at. %) at the GB accompanied with a significant depletion of Cr. At this GB region, Mn also enriches (the peak concentration reaches ∼31.1 at. %) while Fe and Co are depleted. From the perspective of the GB plane normal, the Ni 25 at. % isocomposition surface in Fig. 6(d) and the Cr 15 at. % isocomposition surface in Fig. 6(e) reveal graphically and directly the segregation of Ni and depletion of Cr at the same GB regions. The isocomposition surfaces of Ni and Cr take the shape of strips parallel to each other. Ni segregation together with the Cr depletion occupy part of the GB plane. The 1D composition profile within the GB plane in Fig. 6(f) shows that Ni and Cr show antivariation trend while Mn shows a synchronous and similar variation trend with Ni in their GB compositions. The opposite segregation behavior of Ni

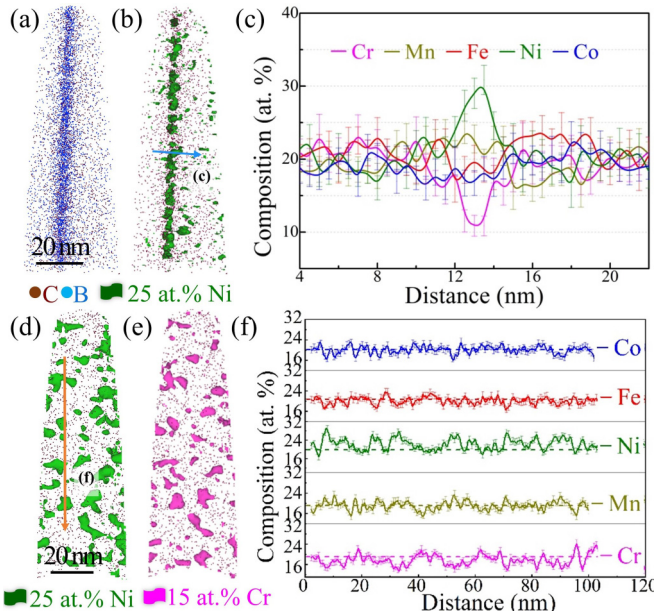

FIG. 5. (a) The atom map of the tip containing a general high-angle GB of 25.6° with C and B atoms, (b) the Ni 25 at. % isocomposition surfaces, (c) the 1D composition profile along the direction in (b); (d) the Ni 25 at. % isocomposition surfaces and (e) Cr 15 at. % isocomposition surfaces in the GB plane and (f) the 1D composition profile along the direction indicated in (d); the dashed lines indicate the corresponding bulk compositions. (a), (b) is viewed with the GB edge on and (d), (e) is viewed along the normal of the GB plane.

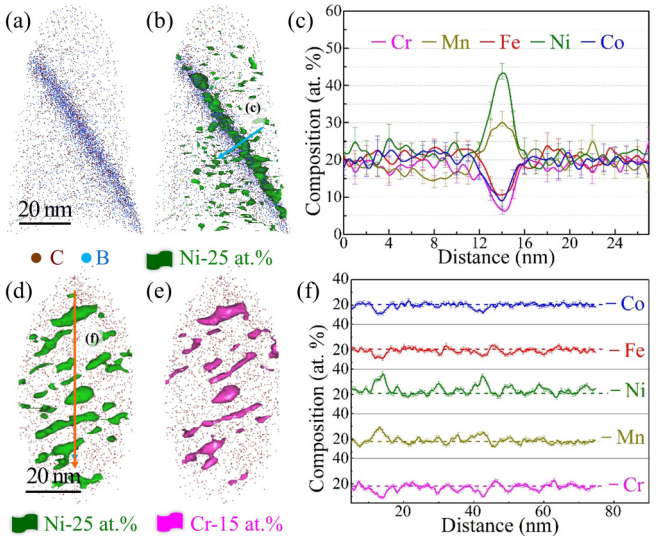

FIG. 6. (a) The atom map of the tip containing a general high-angle GB of 44° with C and B atoms, (b) the Ni 25 at. % isocomposition surfaces, (c) the 1D composition profile along the direction in (b); (d) the Ni 25 at. % isocomposition surfaces and (e) Cr 15 at. % isocomposition surfaces in the GB plane and (f) the 1D composition profile along the direction indicated in (d); the dashed lines indicate the corresponding bulk compositions. (a), (b) is viewed with the GB edge on and (d), (e) is viewed along the normal of the GB plane.

and Cr is also observed in Fe-Ni-Cr systems with little or no Mn content [62] that indicates a strong origin for their antivariation behavior observed here.

The general high-angle GB of 48° also attracts the impurity C and B as well as the primary component Ni as demonstrated by the side views of C and B atom map in Fig. 7(a) and the Ni 25 at. % isocomposition surface in Fig. 7(b). The 1D composition profile across the GB in Fig. 7(c) reveals that there are significant enrichment of Ni (the peak GB concentration is ∼33 at. %), slight enrichment of Mn (the peak GB concentration is ∼22.6 at. %), and depletion of Cr, Fe, and Co at the GB. Similar to the above introduced GBs, the segregation or depletion along the GB of 48° is not homogeneous but occurs at some local regions. The Ni 25 at. % [Fig. 7(d)] and Cr 15 at. % [Fig. 7(e)] isocomposition surfaces in the GB plane demonstrate the heterogeneous and special GB chemistry. To be specific, the concomitant Ni segregation and Cr depletion arising at the same places are exhibited as a certain elongated pattern at the GB. Figure 7(f) reveals the GB composition of all elements more clearly by analyzing the 1D composition profile along the orange arrow in Fig. 7(d) within the GB plane. Ni and Mn cosegregate with a similar variation trend in the GB compositions, which is opposite to that of Cr.

Along with the high segregations of Ni and Mn at the general high-angle GBs (e.g., misorientations of 44° and 48°), there is a certain pattern of the elemental redistribution in accordance with our early results [20]. The compositional modulation of Ni and Mn at these general high-angle GBs is a characteristic feature of spinodal decomposition. The local elemental enrichment is high enough to shift the GB state into a spinodal regime thermodynamically and then the GB segregations can act as precursor states for spinodal decomposition [17,19,20,49].

IV. DISCUSSION

A. Relationship between GB segregations and GB misorientations

In the current experiments, the GBs of different characters show different levels of segregation of the principal substitutional elements after aging treatment. The segregation levels of the interstitial C and B should also depend on the GB characters [63], but their concentrations are far lower (about two orders of magnitude) than the principal elements and have no obvious varying trend. So, GB segregations of C and B are not discussed here. The average composition of the Ni segregation regions at the GBs is displayed in Fig. 8(a). The bulk composition in the grain interior (taken as GB of 0°) was employed here as a reference for comparison. Among the five components, Ni shows the highest enrichment and Cr shows the highest depletion for all the GBs. Ni and Mn show a similar rising trend while Cr, Fe, and Co possess a similar decreasing trend correspondingly in their GB compositions. The segregations of Ni and Mn at the high-angle GBs are strong, but only little amount of them segregate at the low-angle GBs. Besides, there are some abnormally low values at some special high-angle GBs, such as the TB and the vicinal $\Sigma 29b$ GB. The compositions at the TB are almost equal to that in the grain interior except for very little enrichment of Ni.

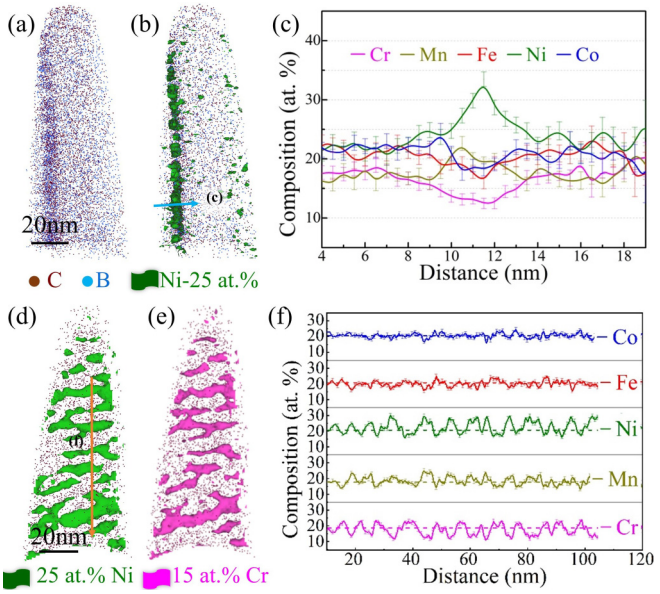

FIG. 7. (a) The atom map of the tip containing a general high-angle GB of 48° with C and B atoms, (b) the Ni 25 at. % isocomposition surfaces, (c) the 1D composition profile along the direction in (b); (d) the Ni 25 at. % isocomposition surfaces and (e) Cr 15 at. % isocomposition surfaces in the GB plane and (f) the 1D composition profile along the direction indicated in (d); the dashed lines indicate the corresponding bulk compositions. (a), (b) is viewed with the GB edge on and (d), (e) is viewed along the normal of the GB plane.

The above Ni 25 at. % isocomposition surfaces of all the samples imply that Ni segregations do not occupy the entire GB plane as sketched in Fig. 8(b). Moreover, the shapes of Ni segregation regions at the GB are usually quite thin because their sizes along the normal of the GB plane are much smaller than their sizes in the GB plane. Thus, we employed the area fraction of Ni segregation per unit GB area to further measure the extent of Ni segregation at the GBs in Fig. 8(c). The area fractions are all smaller than 100% as the Ni segregation never takes up the entire GB plane. Based on these area analyses, there is no segregation in grain interior and almost no segregation at the TBs. Small segregation area was observed at limited regions of the low-angle GB, vicinal CSL GB and the general high-angle GBs of low misorientation angle. For general high-angle GBs of higher misorientation angles, the area fraction of Ni segregation regions can reach higher than 50% per unit GB area implying a high Ni segregation.

B. Relationship between GB segregation and GB energy

According to the results summarized in Fig. 8, the GB segregation has a strong correlation with the GB nature. Especially, it appears that the GB segregation is sensitive to the misorientation angle of the GBs. Yet, there are a number of variables to describe GBs crystallographically, such as the index of the GB plane, the rotation axis, the GB misorientation angle, and so on. For simplicity and clarity, the structure-dependent GB energy is employed here to reveal the correlation between the GB nature and segregation. Previous studies has revealed that GB energy increases with the misorientation angle with the exemption of some special CSL GBs [64,65]. The current similar varying trend of Ni and Mn segregation amount [Fig. 8(c)] implies that the level of segregations closely relates to the GB energy.

Such a relationship between the GB energy, GB misorientation angle, and GB segregation level can be described by using an atomic density parameter, as a first-order measure of the GB nature. The density-based thermodynamic model for GBs is presented in Sec. III. A detailed derivation of this mode can be found in Ref. [48]. Here, the GB density ρ^{GB} is related to the GB excess free volume ΔV and represents the deviation from a defect-free bulk structure as discussed in previous studies [53]. In fact, we have a linear relation $\Delta V \propto (1 - \rho^{GB})$, i.e., a GB with a lower density should have a higher excess free volume [48]. Similar to the excess free volume, the GB density is an average quantity within the GB plane [66]. Thus in the current-density based model we neglect the structural heterogeneity within the GB plane. The current-density based model has been successfully applied to study Mn segregation to the GBs in FeMn alloys [49].

In the current thermodynamic description, Eqs. (3) and (5) give the direct relationship between the initial GB energy γ and the GB composition X_B^{GB} when it is in contact with a given bulk with the composition X_B^B. In general, the level of the segregation depends on (i) the difference between the GB free energies for solute and solvent atoms as well as (ii) the tendency for mixing between them, as reflected in the Gibbs free-energy formulation [Eq. (1)] and the segregation isotherms

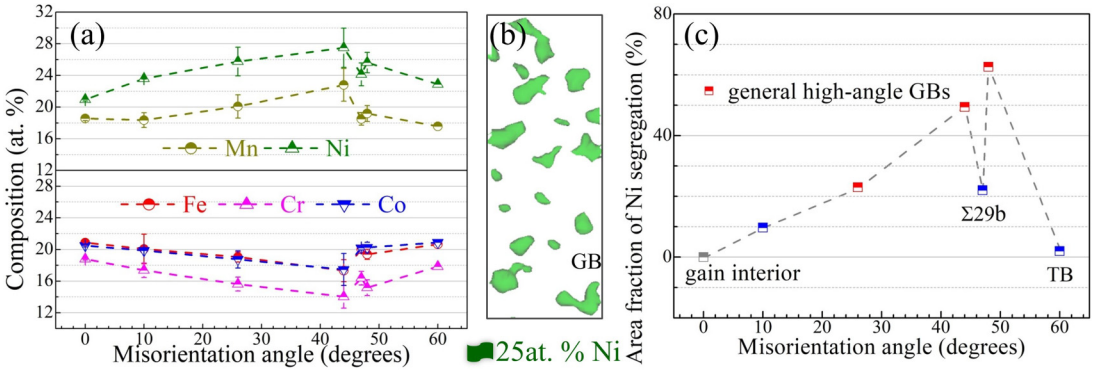

FIG. 8. (a) The average composition of each component in Ni segregation areas at different GBs; (b) a sketch for Ni 25 at. % isocomposition surfaces; (c) the area fraction of Ni segregation regions per unit GB area for different GBs. The misorientation angle of 0° refers to grain interior.

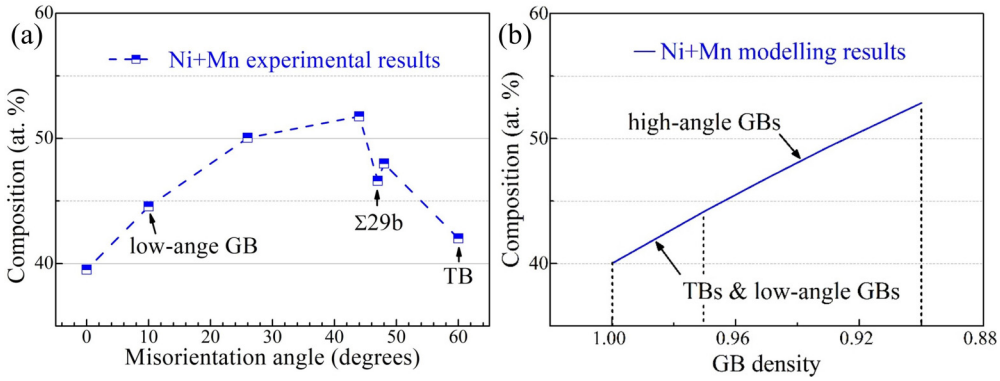

FIG. 9. (a) The experimental results for the average composition of Ni, Mn assembly in Ni segregation areas for different GBs; (b) the modeling results for the composition of Ni, Mn assembly with different GB density.

[Eq. (5)]. The first driving force in Eq. (5), also known as ideal segregation energy, is equal to $\Delta E^B(\rho^{GB^2}-1)+(\Delta K^B+p\Delta V^B-T\Delta S^B)(\rho^{GB}-1)$ which is the only driving force in Langmuir-McLean isotherm [Eq. (6)]. This energy contribution reflects the difference in the GB and bulk environment. From this relation, it is clear that for a GB with a lower density, the deviation from the bulk energy increases and thus the driving force for segregation increases as well. The remaining terms inside the exponential function $\Omega(\rho^{GB^2}-1)+2\Omega[X_B^B-\rho^{GB^2}X_B^{GB}]$ is related to the interaction between the solute and solvent atoms in a binary system. It is important to note that the latter contribution does also include a term which depends on the GB composition X_B^{GB}. Using the current model, we show that the ideal segregation energy and the mixing enthalpy can both have a strong dependence on the GB nature represented by the density parameter ρ^{GB}. This of course depends on the significance of ΔE^B and Ω. If the second term vanishes ($\Omega=0$), Eq. (5) reduces to the Langmuir-McLean isotherm [54] [Eq. (6)] but includes the dependency of segregation isotherms on the GB density.

In order to perform a qualitative study of the segregation behavior and its relation to the initial GB energy in the current HEA, a simplification of the multicomponent system is necessary. According to the experimental results, the main segregating elements are Ni and Mn while Fe, Cr, and Co are depleted from the GBs. Considering the facts that (i) the initial system is equiatomic, (ii) a single-phase substitutional FCC structure was characterized for the current alloy and (iii) the segregating and depleting elements at the GB each follow a very similar trend [see Fig. 9(c)], one can simplify the segregation problem to a semi-binary system with initial composition (Fe, Cr, Co)(Ni, Mn) in which (Ni, Mn) segregate against (Fe, Cr, Co). This means in our thermodynamic notations for a binary AB system, $B\equiv$ (Ni, Mn) is the "solute mixture" and $A\equiv$ (Fe, Cr, Co) is the "solvent mixture." Using this simplification, we can extract the enthalpy and entropy of the solute and solvent mixtures, necessary for our thermodynamics analysis, from the available databases. For the potential energies, the cohesive energy of each element is taken and we apply $K_i^B+pV_i^B=H_i^B-E_i^B$. The enthalpy and entropy of FCC_A1 (Ni, Mn) and (Fe, Cr, Co) mixtures at 723 K are $H_B^B=10.3$ kJ/mol, $S_B^B=68.5$ J/mol/K, $H_A^B=20.0$ kJ/mol, $S_A^B=67.1$ J/mol/K, respectively. These data are extracted from THERMOCALC TCFE9 database [67]. In order to obtain the potential energy of these mixtures the cohesive energies of individual elements are averaged that gives $E_B^B=-355.0$ and $E_A^B=-410.7$, respectively [68]. Based on these values, $\Delta E^B=55.7$ kJ/mol, $\Delta K^B+p\Delta V^B=-66.4$ kJ/mol, and $\Delta S^B=1.4$ J/mol/K are obtained.

For the mixing enthalpy coefficient Ω [Eq. (2)] one can use a similar averaging logic. Here the bonding energies of (Ni, Mn) solute mixture and (Fe, Cr, Co) solvent mixture can be calculated as $\Omega_{BB}\equiv\Omega_{\mathrm{NiMn}}$ and $\Omega_{AA}\equiv\Omega_{\mathrm{FeCrCo}}$. For the pair bonding energies we have

$$\Omega_{ij}=4\Delta H_{ij}. \tag{8}$$

The mixing energy coefficient can be approximated by averaging all possible mixing pairs in which Ni and Mn replace Fe, Cr, or Co atoms. For this scenario:

$$\begin{aligned}\Omega=\Omega_{AB}\equiv\tfrac{1}{9}(&\Omega_{\mathrm{NiCr}}+\Omega_{\mathrm{NiCo}}+\Omega_{\mathrm{CrCo}}+\Omega_{\mathrm{FeNi}}+\Omega_{\mathrm{FeCo}}\\&+\Omega_{\mathrm{FeCr}}+\Omega_{\mathrm{MnCr}}+\Omega_{\mathrm{MnCo}}+\Omega_{\mathrm{FeMn}})\\&-(0.4\Omega_{\mathrm{NiMn}}+0.6\Omega_{\mathrm{FeCrCo}}).\end{aligned} \tag{9}$$

A further approximation also is possible in which higher-order exchange possibilities can be explored. These are, however, omitted in the current analysis for simplicity and due to lack of information. The input values required to calculate Eq. (9) are listed in Table I. These data are extracted from THERMOCALC TCFE9 database [67]. The enthalpy of mixing for simplified equiatomic (Ni, Mn) and (Fe, Cr, Co) solute and solvent mixtures with FCC_A1 structure at 723 K are

TABLE I. Enthalpy of mixing for binary alloys based on THERMOCALC TCFE9 database. These values are used to calculate the mixing enthalpy of the mixture. The units are kJ/mol.

	Mn	Fe	Cr	Co
Ni	−4.9	−4.9	1.3	−1.6
Mn		−2.0	−4.8	−1.8
Fe			2.7	−2.9
Cr				4.5

$H_B^B = -4.9$ and $H_A^B = +3.2$ J/mol, respectively. A negative enthalpy of mixing for Ni and Mn (the solute mixture) indicates the tendency of these elements to attract each other while for the Fe, Cr, and Co (the solvent mixture) the enthalpy of mixing is positive with the tendency of demixing. For our simplified alloy, we obtain $\Omega = -3.9$ kJ/mol. Comparing this result against the largely positive potential energy and the negative enthalpy of mixing for the NiMn solid solution one may expect a decomposition of this solid solution when the appropriate heat treatment conditions are provided. In fact, NiMn ordered phase formed in the same alloy after heat treatment at 500 °C for a long period of time [45]. GB segregation of Ni and Mn evidenced in the current study can accelerate the decomposition kinetics of this HEA at GBs. Interestingly, the CrMn mixture has a negative enthalpy of mixing, similar to the NiMn (Table I). The Mn and Cr atoms, however, are found to show an antivariation at the GBs. Here it is possible that opposite segregation of Ni and Cr affects the segregation behavior of Mn. The opposite segregation of Ni and Cr is also observed in other Fe-Ni-Cr systems with little or no Mn content [62].

Using these thermodynamic values, we obtain the GB segregation level as a function of GB density based on Eq. (5). Figure 9 shows the results from the current model versus the experimental measurements. The solid line in Fig. 9(a) presents the experimental results recomputed from Fig. 8(a) for the semibinary system (Fe, Cr, Co)(Ni, Mn). Here we simply add the concentration of Ni and Mn as solute atoms and Fe, Cr, and Co, as solvent atoms. In terms of the solute segregation, a similar trend has been observed in the experimental data and the density-based thermodynamic modeling when it is studied as a function of the relative GB density. We have considered $\rho^{GB} \in [0.9,\ 1]$ in our modeling calculations. The values for the GB density represent its deviation from the bulk structure ($\rho^B = 1$). Although it is difficult to quantify ρ^{GB} values, the relationships among the GB energy, excess free volume and misorientation angle have been studied intensively. Aaron and Bolling [53] found that the excess free volume of different GBs is proportional to their misorientation angle. For a low-angle GB, they have shown that

$$\Delta V = \alpha_0 \theta(\alpha_1 - \ln\theta), \tag{10}$$

where a higher excess free volume (equivalent to a lower GB density) results from a larger misorientation angle θ. Here α_0 and α_1 are materials parameters. Equation (10) is obtained based on the Seeger and Haasen [69] and Read and Shockley treatments [70]. Based on this relation and Eq. (4) that describes the relationship between GB density and excess free volume, one can see that a lower GB density is expected for higher misorientation values. While TBs and low-angle GBs are known for their small excess free volume (smaller deviations from the bulk structure), the deviation from the bulk structure increases with increasing misorientation angle and the general high-angle GBs reveal largest deviations from the bulk, showing lowest density. These results are well consistent with the general dependency of the excess free volume and GB energy on the misorientation angle as discussed by Aaron and Bolling [53] and Li [71].

In this study, we have observed only lower Ni segregation at TBs and low-angle GBs but higher segregation of Ni+Mn in disordered high-angle GBs. The current thermodynamic analysis shows that the tendency of Ni and Mn for mixing is indeed the main driving force for segregation in this case. This is further assisted by the fact that Fe, Cr, and Co do not like to mix at high concentrations giving a positive enthalpy of mixing for equiatomic FeCrCo. The density-based model suggests that GB made of higher Ni+Mn content is expected to show lower energy. The higher the initial GB energy, the higher the initial driving force for segregation. For general high-angle GBs (with the exception of special high-angle GBs), lower GB density is expected as they are saturated with the high free volume per unit area. GBs with higher excess free volume (lower density) exhibits higher GB energy [Eq. (3)]. Hence there is a larger driving force for Ni+Mn to segregate to the high-angle GBs. In contrast, low-angle GBs and TBs show almost no excess free volume and a density close to the bulk density that results in lower driving force for GB segregation. The apparent relationship between the GB segregation and GB misorientation is thus due to the essential role of GB energy (density) in the elemental segregation as demonstrated by our density-based model. A further detailed study requires atomistic thermodynamic assessment of HEAs as well as a segregation model for multicomponent systems that can be developed based on the current-density based model.

V. CONCLUSIONS

We systematically investigated the chemical compositions of individual GBs in the equiatomic FeMnNiCoCr HEA after aging treatment using APT technique and thermodynamic modeling. A series of GBs with different misorientations and energies was employed to fully explore the mechanism of nanoscale segregation at the varying GBs. Based on the experimental and modeling results and analysis, the following conclusions can be drawn:

(1) Elemental segregations of different levels are observed at different types of GBs. Almost no segregation occurs at the TB and only Ni enriches slightly at the low-angle GB and the vicinal $\Sigma 29b$ GB. Higher levels of Ni and Mn segregations occur at general high-angle GBs of higher misorientation angles.

(2) Ni and Mn tend to show cosegregation at general high-angle GBs while other elements, i.e., Fe, Co, and Cr, are repelled from the GB region. There is also compositional modulation of Ni and Mn at the GB that can work as possible precursor states for spinodal decomposition. Thermodynamic analysis shows that the main driving force for segregation is the large tendency of Ni and Mn to mix while Fe, Cr, and Co prefer to demix when compared to an equiatomic solution. Especially, the Ni and Cr that have a positive enthalpy of mixing show opposite segregation tendency.

(3) The results of the density-based thermodynamic model by consideration of GB density and elemental mixing enthalpy coincides well with the experimental results. It shows that the GB energy plays a key role in the elemental segregations under thermodynamic equilibrium. GBs with higher energy (lower density or higher excess volume) are stronger traps for solute atoms.

ACKNOWLEDGMENTS

L.L. acknowledges the financial support from Alexander von Humboldt Stiftung. R.D.K. acknowledges the financial support from German Research Foundation (DFG) within the Heisenberg programme, Project No. DA 1655/2-1. The authors would like to thank F. Schlüter, M. Nellessen, K. Angenendt, A. Sturm, and U. Tezins for EBSD, FIB, and APT experiments.

[1] A. P. Sutton and R. W. Balluffi, *Interfaces in Crystalline Materials* (Clarendon Press, Oxford, 1995).

[2] R. Kirchheim, Reducing grain boundary, dislocation line and vacancy formation energies by solute segregation. I. Theoretical background, Acta Mater. **55**, 5129 (2007).

[3] M. A. Gibson and C. A. Schuh, Segregation-induced changes in grain boundary cohesion and embrittlement in binary alloys, Acta Mater. **95**, 145 (2015).

[4] M. Yamaguchi, M. Shiga, and H. Kaburaki, Grain boundary decohesion by impurity segregation in a nickel-sulfur system, Science **307**, 393 (2005).

[5] J. Luo, H. Cheng, K. M. Asl, C. J. Kiely, and M. P. Harmer, The role of a bilayer interfacial phase on liquid metal embrittlement, Science **333**, 1730 (2011).

[6] C. T. Liu, C. L. White, and J. A. Horton, Effect of boron on grain-boundaries in Ni_3Al, Acta Metall. **33**, 213 (1985).

[7] J. B. Seol, J. W. Bae, Z. M. Li, J. C. Han, J. G. Kim, D. Raabe, and H. S. Kim, Boron doped ultrastrong and ductile high-entropy alloys, Acta Mater. **151**, 366 (2018).

[8] R. Q. Wu, A. J. Freeman, and G. B. Olson, First principles determination of the effects of phosphorus and boron on iron grain boundary cohesion, Science **265**, 376 (1994).

[9] T. Chookajorn, H. A. Murdoch, and C. A. Schuh, Design of stable nanocrystalline alloys, Science **337**, 951 (2012).

[10] J. Hu, Y. N. Shi, X. Sauvage, G. Sha, and K. Lu, Grain boundary stability governs hardening and softening in extremely fine nanograined metals, Science **355**, 1292 (2017).

[11] E. Wachowicz, T. Ossowski, and A. Kiejna, Cohesive and magnetic properties of grain boundaries in bcc Fe with Cr additions, Phys. Rev. B **81**, 094104 (2010).

[12] K. S. Ming, L. L. Li, Z. M. Li, X. F. Bi, and J. Wang, Grain boundary decohesion by nano-clustering Ni and Cr separately in CrMnFeCoNi high-entropy alloys, Sci. Adv. **5**, eaay0639 (2019).

[13] R. Dong, J. Li, T. Zhang, R. Hu, and H. Kou, Elements segregation and phase precipitation behavior at grain boundary in a Ni-Cr-W based superalloy, Mater. Charact. **122**, 189 (2016).

[14] M. de Hass and J. Th. M. De Hosson, Grain boundary segregation and precipitation in aluminium alloys, Scr. Mater. **44**, 281 (2001).

[15] P. J. Clemm and J. C. Fisher, The influence of grain boundaries on the nucleation of secondary phases, Acta Metall. **3**, 70 (1955).

[16] M. Kuzmina, D. Ponge, and D. Raabe, Grain boundary segregation engineering and austenite reversion turn embrittlement into toughness: Example of a 9 wt.% medium Mn steel, Acta Mater. **86**, 182 (2015).

[17] A. Kwiatkowski da Silva, D. Ponge, Z. Peng, G. Inden, Y. Lu, A. Breen, B. Gault, and D. Raabe, Phase nucleation through confined spinodal fluctuations at crystal defects evidenced in Fe-Mn alloys, Nat. Commun. **9**, 1137 (2018).

[18] D. Raabe, S. Sandlöbes, J. Millán, D. Ponge, H. Assadi, M. Herbig, and P. P. Choi, Segregation engineering enables nanoscale martensite to austenite phase transformation at grain boundaries: A pathway to ductile martensite. Acta Mater. **61**, 6132 (2013).

[19] H. Zhao, F. De Geuser, A. Kwiatkowski da Silva, A. Szczepaniak, B. Gault, D. Ponge, and D. Raabe, Segregation assisted grain boundary precipitation in a model Al-Zn-Mg-Cu alloy, Acta Mater. **156**, 318 (2018).

[20] L. L. Li, Z. M. Li, A. Kwiatkowski da Silva, Z. R. Peng, H. Zhao, B. Gault, and D. Raabe, Segregation-driven grain boundary spinodal decomposition as a pathway for phase nucleation in a high entropy alloy, Acta Mater. **178**, 1 (2019).

[21] P. Lejček, *Grain Boundary Segregation in Metals* (Springer Science & Business Media, Heidelberg, 2010).

[22] P. Lejček and S. Hofmann, Thermodynamics and structural aspects of grain boundary segregation, Crit. Rev. Solid State Mater. Sci. **20**, 1 (1995).

[23] W. T. Xing, A. R. Kalidindi, D. Amram, and C. A. Schuh, Solute interaction effects on grain boundary segregation in ternary alloys, Acta Mater. **161**, 285 (2018).

[24] V. I. Razumovskiy, S. V. Divinski, and L. Romaner, Solute segregation in Cu: DFT vs. experiment, Acta Mater. **147**, 122 (2018).

[25] M. P. Seah and E. D. Hondros, Grain boundary segregation, Proc. Roy. Soc. Lond. A **335**, 191 (1973).

[26] R. Guillou, M. Guttmann, and P. Dumoulin, Role of molybdenum in phosphorus-induced temper embrittlement of 12% Cr martensitic stainless steel, Metal Sci. **15**, 63 (1981).

[27] T. Watanabe, S. Kitamura, and S. Karashima, Grain boundary hardening and segregation in alpha Iron-Tin alloy, Acta Metall. **28**, 455 (1980).

[28] S. Suzuki, K. Abiko, and H. Kimura, Phosphorus segregation related to the grain boundary structure in an Fe-P alloy, Scr. Metall. **15**, 1139 (1981).

[29] H. Gleiter, The segregation of copper at high angle grain boundaries in lead, Acta Metall. **18**, 117 (1970).

[30] C. R. M. Grovenor and C. M. F. Rae, A new method for observing the anisotropy of Bi segregation to Cu grain boundaries, Scr. Metall. **15**, 1305 (1981).

[31] X. Zhou, X. X. Yu, T. Kaub, R. L. Martens, and G. B. Thompson, Grain boundary specific segregation in nanocrystalline Fe(Cr), Sci. Rep. **6**, 34642 (2016).

[32] M. A. Meyers and K. K. Chawla, *Mechanical Behavior of Materials* (Cambridge University Press, Cambridge, 2008).

[33] S. J. Dillon, M. P. Harmer, and G. S. Rohrer, Influence of interface energies on solute partitioning mechanisms in doped aluminas, Acta Mater. **58**, 5097 (2010).

[34] R. Kirchheim, Reducing grain boundary, dislocation line and vacancy formation energies by solute segregation: II. Experimental evidence and consequences, Acta Mater. **55**, 5139 (2007).

[35] B. Cantor, I. T. H. Chang, P. Knight, and A. J. B. Vincent, Microstructural development in equiatomic multicomponent alloys, Mater. Sci. Eng. A **375–377**, 213 (2004).

[36] J. W. Yeh, S. K. Chen, S. J. Lin, J. Y. Gan, T. S. Chin, T. T. Shun, C. H. Tsau, and S. Y. Chang, Nanostructured high-entropy alloys with multiple principal elements: Novel alloy design concepts and outcomes, Adv. Eng. Mater. **6**, 299 (2004).

[37] B. Gludovatz, A. Hohenwarter, D. Catoor, E. H. Chang, E. P. George, and R. O. Ritchie, A fracture-resistant high-entropy alloy for cryogenic applications, Science **345**, 1153 (2014).

[38] Z. M. Li, K. G. Pradeep, Y. Deng, D. Raabe, and C. C. Tasan, Metastable high-entropy dual-phase alloys overcome the strength-ductility trade-off, Nature (London) **534**, 227 (2016).

[39] Y. Zhang, T. T. Zuo, Z. Tang, M. C. Gao, K. A. Dahmen, P. K. Liaw, and Z. P. Lu, Prog. Mater. Sci. **61**, 1 (2014).

[40] B. Schuh, F. Mendez-Martin, B. Völker, E. P. George, H. Clemens, R. Pippan, and A. Hohenwarter, Mechanical properties, microstructure and thermal stability of a nanocrystalline CoCrFeMnNi high-entropy alloy after severe plastic deformation, Acta Mater. **96**, 258 (2015).

[41] F. Otto, A. Dlouhý, K. G. Pradeep, M. Kuběnová, D. Raabe, G. Eggeler, and E. P. George, Decomposition of the single-phase high-entropy alloy CrMnFeCoNi after prolonged anneals at intermediate temperatures, Acta Mater. **112**, 40 (2016).

[42] N. Zhou, T. Hu, and J. Luo, Grain boundary complexions in multicomponent alloys: Challenges and opportunities, Curr. Opin. Solid State Mater. Sci. **20**, 268 (2016).

[43] M. Vaidya, K. G. Pradeep, B. S. Murty, G. Wilde, and S. V. Divinski, Bulk tracer diffusion in CoCrFeNi and CoCrFeMnNi high entropy alloys, Acta Mater. **146**, 211 (2018).

[44] M. Vaidya, K. G. Pradeep, B. S. Murty, G. Wilde, and S. V. Divinski, Radioactive isotopes reveal a non sluggish kinetics of grain boundary diffusion in high entropy alloys, Sci. Rep. **7**, 1 (2017).

[45] Y. J. Li, A. Savan, A. Kostka, H. S. Stein, and A. Ludwig, Accelerated atomic-scale exploration of phase evolution in compositionally complex materials, Mater. Horiz. **5**, 86 (2017).

[46] P. Wynblatt and D. Chatain, Modeling grain boundary and surface segregation in multicomponent high-entropy alloys, Phys. Rev. Mater. **3**, 054004 (2019).

[47] G. B. Thompson, M. K. Miller, and H. L. Fraser, Some aspects of atom probe specimen preparation and analysis of thin film materials, Ultramicroscopy **100**, 25 (2004).

[48] R. Darvishi Kamachali, A model for grain boundary thermodynamics, arXiv:1907.12231.

[49] R. Darvishi Kamachali, A. Kwiatkowski da Silva, E. McEniry, D. Ponge, B. Gault, J. Neugebauer, and D. Raabe, Segregation–assisted spinodal and transient spinodal phase separation at grain boundaries, arXiv:1905.07970.

[50] J. D. van der Waals, The thermodynamic theory of capillarity under the hypothesis of a continuous variation of density, J. Stat. Phys. **20**, 200 (1979).

[51] J. W. Cahn and J. E. Hilliard, Free energy of a nonuniform system. I. Interfacial free energy, J. Chem. Phys. **28**, 258 (1958).

[52] D. A. Porter, K. E. Easterling, and M. Sherif, *Phase Transformations in Metals and Alloys* (revised reprint) (CRC Press, Boca Raton, FL, 2009).

[53] H. Aaron and G. Bolling, Free volume as a criterion for grain boundary models, Surf. Sci. **31**, 27 (1972).

[54] D. MacLean, *Grain Boundaries in Metals* (Clarendon Press, Oxford, 1957).

[55] R. H. Fowler and E. A. Guggenheim, *Statistical Thermodynamics* (Macmillan, New York, 1939).

[56] Z. Wang, I. Baker, W. Guo, and J. D. Poplawsky, The effect of carbon on the microstructures, mechanical properties, and deformation mechanisms of thermo-mechanically treated $Fe_{40.4}Ni_{11.3}Mn_{34.8}Al_{7.5}Cr_6$ high entropy alloys, Acta Mater. **126**, 346 (2017).

[57] B. Gault, M. P. Moody, J. M. Cairney, and S. P. Ringer, *Atom Probe Microscopy* (Springer Science & Business Media, 2012), Vol. 160.

[58] D. Seidman, Solute-atom segregation at internal interfaces on an atomic scale: Atom-probe experiments and computer simulations, Mater. Sci. Eng. A **137**, 57 (1991).

[59] M. Herbig, M. Kuzmina, C. Haase, R. K. W. Marceau, I. Gutierrez-Urrutia, D. Haley, D. A. Molodov, P. Choi, and D. Raabe, Grain boundary segregation in Fe–Mn–C twinning-induced plasticity steels studied by correlative electron backscatter diffraction and atom probe tomography, Acta Mater. **83**, 37 (2015).

[60] R. Kirchheim, Grain coarsening inhibited by solute segregation, Acta Mater. **50**, 413 (2002).

[61] D. Scheiber, V. I. Razumovskiy, P. Puschnig, R. Pippan, and L. Romaner, Ab initio description of segregation and cohesion of grain boundaries in W–25at.% Re alloys, Acta Mater. **88**, 180 (2015).

[62] H. Li, S. Xi, W. Q. Liu, T. G. Liu, and B. X. Zhou, Atomic scale study of grain boundary segregation before carbide nucleation in Ni–Cr–Fe Alloys, J. Nucl. Mater. **439**, 57 (2013).

[63] M. Herbig, D. Raabe, Y. J. Li, P. Choi, S. Zaefferer, and S. Goto, Atomic-Scale Quantification of Grain Boundary Segregation in Nanocrystalline Material, Phys. Rev. Lett. **112**, 126103 (2014).

[64] D. L. Olmsted, S. M. Foiles, and E. A. Holm, Survey of computed grain boundary properties in face-centered cubic metals: I. Grain boundary energy, Acta Mater. **57**, 3694 (2009).

[65] D. Wolf, Structure-energy correlation for grain boundaries in F.C.C. metals—III. Symmetrical tilt boundaries, Acta Metall. Mater. **38**, 781 (1990).

[66] G. Gunter and L. S. Shvindlerman, *Grain Boundary Migration in Metals: Thermodynamics, Kinetics, Applications* (CRC Press, Boca Raton, FL, 2009).

[67] THERMO-CALC SOFTWARE TCFE Steels/Fe-alloys database version 9 (accessed 23 March 2019).

[68] C. Kittel, *Introduction to Solid State Physics,* Vol. 8 (Wiley, New York, 1976).

[69] A. Seeger and P. Haasen, Density changes of crystals containing dislocations, Philos. Mag. **3**, 470 (1958).

[70] W. T. Read and W. Shockley, Dislocation models of crystal grain boundaries, Phys. Rev. **78**, 275 (1950).

[71] J. C. Li, High-angle tilt boundary—a dislocation core model, J. Appl. Phys. **32**, 525 (1961).